# Defective Electroluminescence Image Generation for Data Imbalance in Solar Cell Defect Inspection

Ziai Zhou , Jiacheng Jiang , and Jinxia Zhang , *Member, IEEE*

*Abstract*—The utilization of high-resolution electroluminescence (EL) images for defect inspection in photovoltaic modules has gained significant popularity. However, there are limited works on the imbalance problem in the EL images of the photovoltaic modules, specifically that the number of defective images is substantially less than the number of normal images. To address the above problem, a fast defective EL image generation method is proposed in this article. To accurately extract the defective region, a normal image, which is the most similar to the defective image, needs to be identified. First, an image type classification network is proposed to recognize the normal images with the same type (monocrystalline or polycrystalline) as the defective image. Then, the cosine similarity is further employed to identify the normal image that is most similar to the defective image. After that, the defective template is acquired by comparing the defective image with the identified similar normal image. To quickly generate diverse and rich defective EL images, effective data augmentation methods for EL images are exploited and applied to the defective template. Specifically, small-scale rotation and Gaussian blurring are first introduced to augment the EL images. Finally, the augmented defective templates are merged with any different normal images to produce a large amount of new defective images. The experimental comparison of the proposed defective image generation method with oversampling and data augmentation, which are commonly used for data imbalance, demonstrates that our proposed method can provide richer information and thus outperform other methods with a big gap.

*Index Terms*—Data imbalance, deep learning, defect extraction, electroluminescence (EL) image, photovoltaic (PV) modules.

## I. INTRODUCTION

USING photovoltaic (PV) technology is one of the most straightforward methods for transforming solar energy into electricity power. In recent decades, the worldwide market of PV technology has shown remarkable expansion. The global PV cumulative capacity grew to 1.6 TW in 2023, up from 1.2 TW in 2022 [1]. Solar cells are critical and delicate modules that need utmost caution to safeguard them against potential harm [2]. The occurrence of failures might potentially result in a substantial decrease in the efficiency of PV modules [3].

Electroluminescence (EL) imaging is widely used to inspect defects in solar cells. As a nondestructive and contactless approach, EL imaging offers high-resolution images, thus facilitating the visualization of different defects [4]. Tsai et al. [5] used Fourier image reconstruction to inspect defects in EL images of solar cells. However, this method struggles to inspect complex-shaped defects due to its reliance on shape assumptions. Anwar and Abdullah [6] proposed an algorithm combining anisotropic diffusion filtering and shape analysis to identify defective regions. While it performs well in inspecting microdefects, it ignores some other types of defects.

Machine learning provides an automated, cost-effective, and time-efficient solution to EL defect inspection [7], [8]. Su et al. [9] conducted a comparative analysis of support vector machine and convolutional neural network (CNN) concerning EL defect inspection. The CNN approach achieves high accuracy but exhibits low efficiency compared to traditional methods. Akram et al. [10] reached a harmonious equilibrium between precision and effectiveness successfully in the classification of PV defects using a lightweight CNN. Hassan and Dhimish [11], [12] proposed a novel approach to automated PV defect inspection by developing four different deep learning models and a CNN architecture, which combines mean pooling and max pooling to capture distinctive features of defects on solar cells. Fioresi et al. [13] demonstrated a sophisticated deep learning model that individually classifies and localizes four different combined defect categories.

Although there have been many studies on defect inspection of solar cells, few studies have considered the issue of data imbalance. For solar cells, there is a relatively lower quantity of defective images compared to normal images, thus leading to the data imbalance. Using an imbalanced dataset for model training often yields suboptimal training outcomes, since the results tend to exhibit bias toward the majority class while the minority samples are either undiscovered, ignored, or considered as noise [14]. Misclassifying defective solar cells as nondefective ones can cause abnormal PV module operation, significantly impacting output efficiency. Consequently, the need to achieve effective defect inspection under an imbalanced dataset becomes a pressing concern.

Oversampling and data augmentation are effective techniques to expand the dataset in the field of EL defect inspection,

Ziai Zhou and Jiacheng Jiang are with the Key Laboratory of Measurement and Control of CSE, Ministry of Education, School of Automation, Southeast University, Nanjing 210096, China (e-mail: 230238499@seu.edu.cn; lanjjc1998@163.com).

Jinxia Zhang is with the Key Laboratory of Measurement and Control of CSE, Ministry of Education, School of Automation, Southeast University, Nanjing 210096, China, and also with the Advanced Ocean Institute of Southeast University, Nanjing 226010, China (e-mail: jinxiazhang@seu.edu.cn).
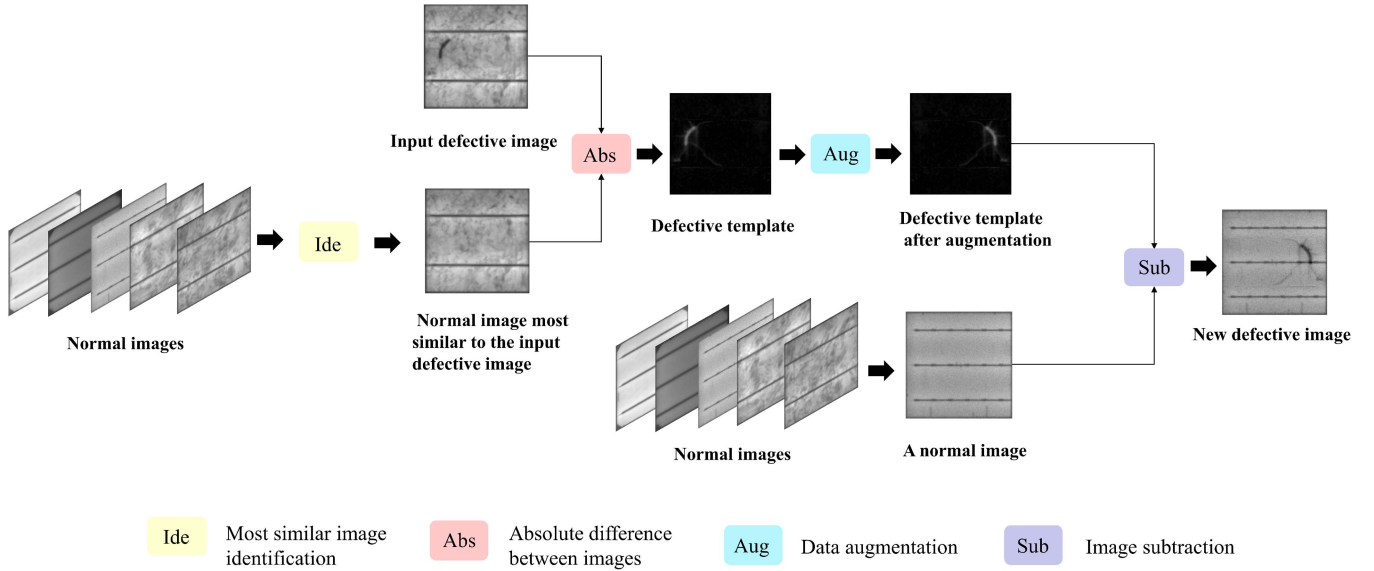
Fig. 1. Process of generating new defective images from the most similar image pairs. The most similar normal image to the input defective image is identified to obtain the defective template, which is combined with a random normal image after data augmentation to create a new defective image.

alleviating the issue of data imbalance. Akram et al. [15] compared three models for the identification of solar cell defects and expanded the original data by four times through rotation and flipping. Zhang et al. [16] trained a deep adoption network using a labeled monocrystalline dataset consisting of 44 photos, but with augmentations, it expanded to over 2000 images. Chen et al. [17] developed a rapid automatic computer vision pipeline to identify defects in EL images and used oversampling to process the training set. Demirci et al. [18] proposed a two-stage procedure for the detection of various EL-based solar cell defects and employed a variety of data augmentation approaches to pay special attention to the defective classes. Su et al. [19] used data augmentation before and during the training stage to evaluate multiple EL defect inspection methods.

Although some works have considered the lack of defective images, few of them focus on explicitly addressing the data imbalance problem. To solve the data imbalance problem, a defective EL image generation method is proposed in this article based on defective region extraction. Experiments demonstrate that our method outperforms classic oversampling and data augmentation, and better copes with the impact of EL data imbalance. The contributions of this work are as follows.

1) An efficient defective EL image generation approach is exploited. First, the most similar normal and defective image pairs are identified based on a proposed image type classification network and cosine similarity. After comparing the image pairs, the defective templates are acquired. Finally, the augmented defective templates are combined with any different normal images to create a large set of new defective images.

2) The effective data augmentation techniques for EL images are exploited by experiments. We first introduce Gaussian blur and small-scale rotation according to the noise and the position of defects to exploit more useful information about defects.

3) The experimental results demonstrate the validity of our method. Specifically, the Balanced Accuracy/Recall/F1 score/G-mean improves by 2.48%/3.36%/2.37%/1.47%, respectively, compared to the optimal results of the commonly used data augmentation and oversampling methods.

The rest of this article is organized as follows. The proposed method and details are described in Section II. The results obtained from the experiments are reported and discussed in Section III. Finally, Section IV concludes this article with the scope of future work.

## II. METHODOLOGY

To address the data imbalance problem, a novel image generation method is proposed in this article through automatically extracting defective regions as the defective template. To accurately extract the defective region, a normal image, which is the most similar to the defective image, needs to be identified since the defective region is computed as the difference between the defective image and the normal image. After exploiting effective data augmentation operations for EL images, the augmented defective templates are merged with any different normal images to efficiently generate a large amount of new defective EL images. The whole process of generating new defective images from the most similar image pairs is shown in Fig. 1.

### A. Similar Normal Image Identification

According to the observation, the backgrounds of both defective images and normal images contain the same elements, such as horizontal gratings, flocculent noises, etc. Thus, defective regions are extracted as the defective template by comparing similar defective and normal image pairs. It is essential to identify the normal image that is most similar to the defective image. However, manually identifying similar normal images poses

TABLE I
PARAMETERS OF LAYERS OF THE PROPOSED IMAGE TYPE CLASSIFICATION NETWORK

| Layer type | Parameters setting |
|---|---|
| Image input | $[300 \times 300 \times 3]$ scaled to the range [0,1] |
| Convolution | 4 $(3 \times 3)$ filers with stride 1, padding 1 [ReLu] |
| Batch normalization | |
| Max pooling | $2 \times 2$ filter with stride 2 |
| Convolution | 8 $(3 \times 3)$ filers with stride 1, padding 1 [ReLu] |
| Batch normalization | |
| Max pooling | $2 \times 2$ filter with stride 2 |
| Convolution | 16 $(3 \times 3)$ filers with stride 1, padding 1 [ReLu] |
| Batch normalization | |
| Max pooling | $2 \times 2$ filter with stride 2 |
| Convolution | 32 $(3 \times 3)$ filers with stride 1, padding 1 [ReLu] |
| Batch normalization | |
| Max pooling | $2 \times 2$ filter with stride 2 |
| Convolution | 32 $(3 \times 3)$ filers with stride 1, padding 1 [ReLu] |
| Batch normalization | |
| Max pooling | $2 \times 2$ filter with stride 2 |
| Adaptive average pooling | output size $7 \times 7$ |
| Fully connected (FC) | 256 [ReLu, 0.5 dropout] |
| Fully connected (FC) | 256 [ReLu, 0.5 dropout] |
| Output | 2 (softmax classifier) |

significant challenges. In addition, EL images for polycrystalline silicon solar cells often exhibit substantial flocculent noises in the backgrounds, making it scarcely possible for the human eyes to discern similarities between images.

An automatic approach is proposed to identify similar images. It is evident that silicon solar cells of the same type (monocrystalline or polycrystalline) exhibit a higher degree of similarity compared to cells of different types. Therefore, an image type classification network is proposed to recognize the image type, which consists of a feature extraction block, an average pooling layer, and a classification head. The architecture of the classification network consists of convolutional layers, pooling layers, batch normalization layers, rectified linear unit (ReLU) function, max pooling layers, fully connected layers, and loss.

In this article, we conduct experiments on an open-sourced EL photovoltaic (ELPV) module cell dataset, which is proposed by Deitsch et al. [7]. Greyscale EL images with dimensions of $300 \times 300 \times 3$ from the ELPV dataset are input to the image type classification network. The features of images are extracted by five feature extraction blocks, which consist of convolutional layer, batch normalization, and max pooling layer. The structure of each feature extraction block is the same while the number of filters is different, which allows the network to gradually extract more detailed features of the images. Batch normalization [20] allows the model to learn optimal input scaling and mean for each layer. Each feature is standardized in a mini-batch by subtracting the mean and dividing the difference by the standard deviation. The pooling layer can increase translation invariance and avoid overfitting.

The classifier consists of three fully connected layers. The dropout rate for the fully connected layer is set to 0.5. Dropout [21] causes dropping out of units randomly in neural networks, which makes the model more effective in handling complex data and reduces the risk of overfitting. After passing through all the layers, the pixel values are transformed into class scores to identify the type of the input EL image. The details of these layers and hyperparameters are listed in Table I.

The method for acquiring the most similar defective and normal image pairs is illustrated in Fig. 2. The proposed image type classification network first classifies the normal images and the input defective images to determine their type. Based on the result of classification, normal images with the same type of defective image are identified. After calculating the cosine similarity between the defective image and each normal image of the same type, the normal image with the highest cosine similarity to the defective image is considered as the most similar image. Fig. 3 illustrates examples of the most similar defective and normal image pairs, where Fig. 3(a) and (c) presents defective silicon solar cells, and Fig. 3(b) and (d) presents their corresponding most similar normal cells. It can be seen that our similar image identification method effectively identifies defective and normal image pairs with the highest degree of similarity.

### B. Defective Image Generation

Image subtraction and absolute difference are useful in detecting disparities between two images. The inclusion of pixel value changes at the edge of the defect region in the image subtraction procedure ensures that the resulting defective template exhibits a more authentic and seamless pixel value transition at the border of defect.

The input defective image, the normal image that is most similar to the defective image, and the defective template acquired by subtraction are denoted as img_d, img_m, and temp, respectively. The acquisition of the defective template is mathematically expressed as follows:

$$\text{temp} = |\text{img\_}d - \text{img\_}m|. \tag{1}$$

Fig. 4 displays several instances of defective templates. The white area of the defective region is visible against the black background. In Fig. 4, a microcrack is a crack that does not influence the current flow over the crack. A fragement is a crack that influences the current flow to the cell interconnect ribbon of the cell. Printing errors are identical to finger interruptions on some cells in a PV module or gridfinger interruptions caused by soldering [22]. It is possible to extract various types of defective regions, including cracks, that are difficult to identify.

To get a richer amount of data, data augmentation is used to augment the defective template. The process of generating new defective images is described as follows:

$$\text{img\_}d^* = \text{img\_}n - \text{temp}^A. \tag{2}$$

We propose an image type classification network to obtain normal images of the same type as the input defective image. The defective image img_d is compared to a set of normal images with the same image type using cosine similarity to find the most similar image img_m. The image subtraction between the similar image pairs derives the defective template temp. After data augmentation for temp, any normal image img_n is randomly selected for image fusion, hence generating a large number of new defective images img_d*. The overall procedure for defective image generation is outlined in Algorithm 1.
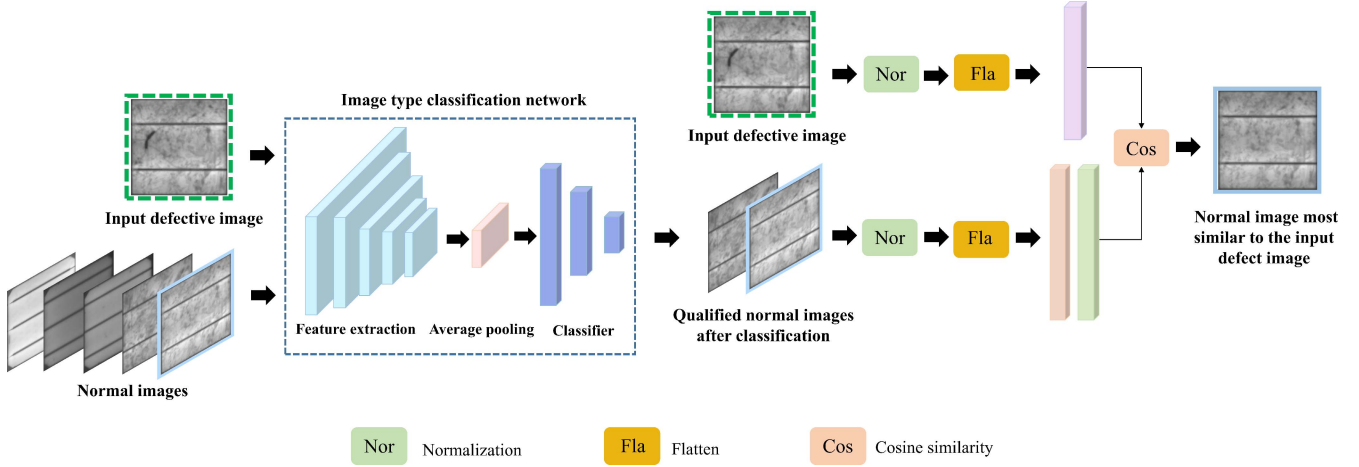
Fig. 2. Process of obtaining the normal image that is most similar to the input defective image. Types of the input defective image and normal images are determined by the image type classification network. After calculating the cosine similarity between the input defective image and each normal image of the same type, the normal image with the highest cosine similarity to the defective image is considered as the most similar image.
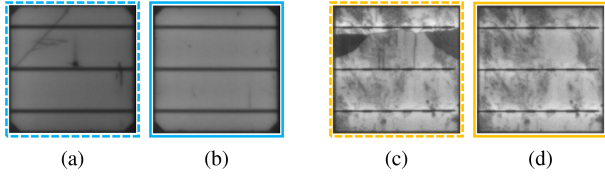


Fig. 3. Examples of most similar defective and normal image pairs. (a) and (c) Defective silicon solar cells. (b) and (d) Corresponding most similar normal cells.
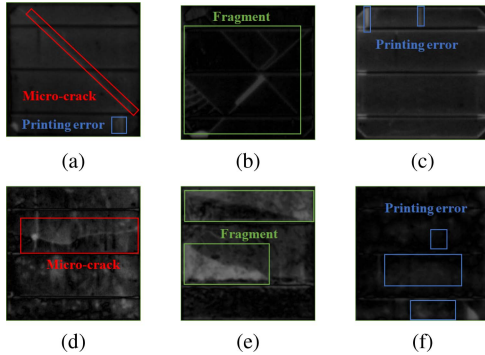


Fig. 4. Examples of templates. (a)–(c) Monocrystalline silicon solar cells. (d)–(f) Polycrystalline silicon solar cells. The defects are marked with rectangular boxes.

## III. EXPERIMENTS

Experiments are conducted to compare the proposed defective EL image generation method with commonly used oversampling and data augmentation methods on a public imbalanced dataset, i.e., ELPV dataset [7] to demonstrate the effectiveness of the proposed method. It is worth noting that all the experimental results were obtained by running seven times and then taking the average to ensure the authenticity and reliability of the results. Some basic parameters we used in the experiments are fixed, where the initial learning rate is 0.01, momentum is 0.9, weight decay is 5e-4, the default loss function is the cross-entropy loss

---

**Algorithm 1:** Defective EL Image Generation Method for Data Imbalance in PV Modules Defect Inspection.

**Input:** A defective EL image $img\_d$;

(1) Propose an image type classification network to obtain normal images of the same type as the defective image.

(2) Calculate cosine similarity to find the most similar normal image $img\_m$ to the defective image.

(3) Use image synthesis in (1) to achieve a defective template $temp$.

(4) Exploit data augmentation for the defective template, denoted as $temp^A$. We first introduce Gaussian blur and small-scale rotation to the EL data set which can provide richer information to the model.

(5) Merge the defective template $temp^A$ with any random normal image $img\_n$ using (2) to obtain a large number of new defective images $img\_d^*$.

**Output:** A large number of newly generated defective images $img\_d^*$;

---

function, and the optimizer is stochastic gradient descent. In the experiment, a pretrained ResNet50 [23] model without data augmentation to inspect the defect is used as the baseline.

### A. Dataset

The ELPV dataset contains 2624 EL images of solar cells with a resolution of $300 \times 300$ pixels, extracted from 44 different PV modules, 18 of which are of the monocrystalline type and 26 of which are of the polycrystalline type. The number of normal images is approximately twice the number of defective ones. Some examples of defective images are shown in Fig. 5.
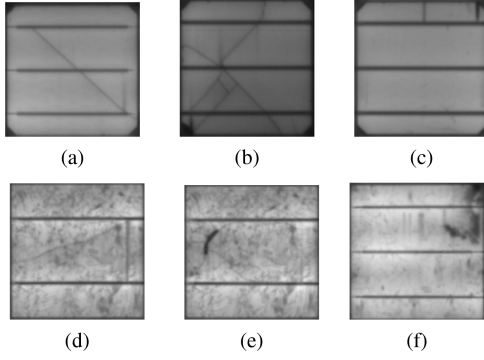
This article has been accepted for inclusion in a future issue of this journal. Content is final as presented, with the exception of pagination.

ZHOU et al.: DEFECTIVE ELECTROLUMINESCENCE IMAGE GENERATION FOR DATA IMBALANCE IN SOLAR CELL DEFECT INSPECTION 5



Fig. 5. Examples of defective images in the ELPV dataset. (a)–(c) Monocrystalline silicon solar cells. (d)–(f) Polycrystalline silicon solar cells.

## B. Evaluation Metrics

Accuracy and error rate are the most frequently used metrics when evaluating classification results [24]. However, both of them are insufficient when dealing with imbalanced dataset, since the resulting value is dominated by the majority group. Therefore, we adopt evaluation metrics commonly used in imbalanced dataset in our experiment, i.e., Balanced Accuracy, Recall, F1 score, and G-mean.

The Balanced Accuracy calculates a more sensitive metric for minority group, which is defined as the arithmetic mean of the proportion of correct predictions for each class. The Balanced Accuracy is calculated as true positive rate (TPR) + true negative rate (TNR) $/2$[25]. TPR, which is also called as Recall, measures the percentage of the positive group that is correctly labeled as positive by the model. TPR is calculated as $TP/(TP + FN)$. TNR measures the percentage of negative group that is correctly predicted to be negative. TNR is calculated as $TN/(TN + FP)$. TP stands for true positive, FP stands for false positive, FN stands for false negative, and TN stands for true negative.

F1 score combines Precision and Recall, which is calculated as $2 \times Recall \times Precision/(Recall + Precision)$ [26]. Precision is calculated as $TP/(TP + FP)$. The G-mean measures performance by the square root of the product of TPR and TNR, which is calculated as $\sqrt{TPR \times TNR}$ [27].

## C. Performance Comparison

Data augmentation employs methods that are experimentally proven effective for EL images, including horizon flipping, vertical flipping, rotations, as well as Gaussian blur with a blur radius of 1 for the training set. Oversampling randomly samples data from the training set to balance the number of defective and normal images. The method, abbreviated as "aug + oversample" for simplicity, not only employs data augmentation methods but also samples defective images from the ELPV dataset. To ensure fair and valid experimental results, the same number of images is used in the experiments of the oversampling method, the aug + oversample method, and our proposed method. The results of different methods are shown in Table II.

| Operation | B_accuracy | Recall | F1 score | G-mean |
|---|---|---|---|---|
| Baseline | 0.8527 | 0.7409 | 0.8144 | 0.8453 |
| Data augmentation | 0.8764 | 0.7999 | 0.8412 | 0.8729 |
| Oversampling | 0.8766 | 0.8291 | 0.8308 | 0.8753 |
| Aug + oversample | 0.8869 | 0.8263 | 0.8505 | 0.8646 |
| Proposed approach | **0.9014** | **0.8627** | **0.8649** | **0.8900** |

The aug + oversample method not only employs data augmentation methods but also samples defective images from ELPV Dataset. The best results are in bold and the second best are in underlined.
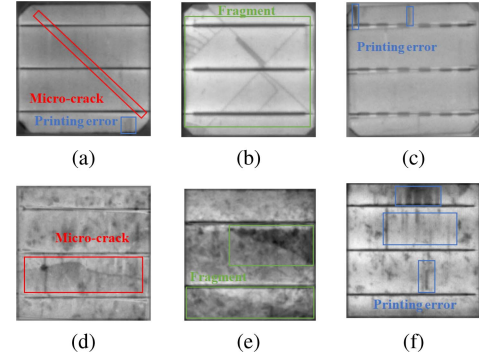


Fig. 6. New defective images generated correspondingly by the defective templates in Fig. 4. The defects are marked with rectangular boxes. (a)–(c) Monocrystalline silicon solar cells. (d)–(f) Polycrystalline silicon solar cells.

In Table II, all the metrics indicate that the proposed method has the best overall performance under the imbalanced dataset. In terms of Balance Accuracy and G-mean, our method outperforms oversampling by 2.48% and 1.47%, respectively. On Recall, our method is well above baseline and data augmentation by at least 6% and outperforms oversampling by 3.36%. The aug + oversample method achieves commendable results in terms of Balanced Accuracy and F1 score. However, the metrics of Recall and G-mean do not exhibit superior performance compared to the application of oversampling methods alone. This could be attributed to the fact that the concurrent application of oversampling and data augmentation to the original ELPV dataset may lead to the proliferation of redundant information, which could potentially diminish the defect inspection performance. The higher Recall indicates that our method can miss fewer defective samples. What is more, the F1 score is also optimal at this time, which indicates that our method can also maintain a better balance between Precision and Recall, thus avoiding skewed prediction.

## D. Visual Effect

Fig. 6 displays six defective image samples generated by the proposed method, each corresponding to a defective template in Fig. 4. Fig. 6(a)–(c) presents the newly generated EL images of monocrystalline silicon solar cells, while Fig. 6(d)–(f) presents the newly generated EL images of polycrystalline silicon solar cells. It is evident that the generated defective images closely

TABLE III
RESULTS OF EL DEFECT INSPECTION FOR ABLATING CORE COMPONENTS OF THE PROPOSED APPROACH

| Operation | B_accuracy | Recall | F1 score | G-mean |
|---|---|---|---|---|
| No augmentation and classification | 0.8726 | 0.7941 | 0.8351 | 0.8680 |
| With augmentation | 0.8786 | 0.8039 | 0.8432 | 0.8743 |
| With classification | 0.8929 | 0.8480 | 0.8543 | 0.8816 |
| Proposed approach | 0.9014 | 0.8627 | 0.8649 | 0.8900 |

TABLE IV
DATA AUGMENTATION EFFECT OF PV CELL IMAGE

| Augmentation operation | B_accuracy | Recall | F1 score | G-mean |
|---|---|---|---|---|
| Baseline | 0.8527 | 0.7409 | 0.8144 | 0.8453 |
| Horizon flip | 0.8751 | 0.7997 | 0.8378 | 0.8718 |
| Vertical flip | 0.8692 | 0.7892 | 0.8301 | 0.8655 |
| Contrast | 0.8460 | 0.7276 | 0.8057 | 0.8733 |
| Blur (radius = 1) | 0.8602 | 0.7759 | 0.8172 | 0.8560 |
| Blur (radius = 2) | 0.8433 | 0.7479 | 0.7940 | 0.8379 |
| Scale | 0.8565 | 0.7591 | 0.8159 | 0.8510 |
| Translate | 0.8565 | 0.7591 | 0.8159 | 0.8510 |
| Rotation_ 3 | 0.8603 | 0.7640 | 0.8213 | 0.8549 |
| Rotation_90 | 0.8630 | 0.7661 | 0.8265 | 0.8577 |
| Rotation_180 | 0.8672 | 0.7794 | 0.8295 | 0.8627 |
| Rotation_270 | 0.8617 | 0.7780 | 0.8186 | 0.8576 |
| Combination | **0.8764** | **0.7999** | **0.8412** | **0.8729** |

The best results are in bold and the second best are in underlined.

resemble the real EL images and clearly show the defective regions. Moreover, the newly generated images effectively present defects that are difficult to identify and truly present the flocculent noises on the EL images of polycrystalline silicon. In addition, our method is computationally lightweight, requiring merely 8 min of processing time on a standard CPU to produce 1000 high-quality defective EL images. The defective image generation process is offline, thereby circumventing the need for computational expenditure during the stage of training and testing.

*E. Ablation Experiments*

Study of the proposed defective EL image generation approach*:* The core operations of our method are image classification performed by the proposed image type classification network and data augmentation of the defective template, of which experiments are conducted to illustrate the effectiveness. The results are shown in Table III.

Based on the proposed defective EL image generation approach, the template augmentation and image type classification network are all removed to get a primary algorithm, which is indicated as no augmentation and classification. The secondary algorithms only combine the template augmentation or image type classification network and are indicated as with augmentation and with classification. The final algorithm is indicated as proposed approach for clarity.

According to all metrics, the final algorithm has the best overall performance with the help of an image type classification network and data augmentation. The secondary algorithms, which only combine the data augmentation or image type classification network, have the median performances. The primary algorithm without data augmentation and a classification network has the worst performance.

We also evaluate the performance of the image type classification network, and experiments show that the accuracy of the proposed image type classification network can achieve almost 100%. The experiment results indicate that the proposed image type classification network can identify the image type perfectly, thus contributing to the template generation.

Study of effective data augmentation methods*:* According to our observation, the defects in the EL image can be anywhere with any orientation. After flipping or rotating, the defects in the image can appear in different positions of the image, thus effectively improving the diversity of defective EL images. Small-scale rotations are first introduced to the EL dataset in this research, which can make the defects in the image move in a small range, thus enhancing the robustness of the model and

providing new information for model training. We also introduce a Gaussian blur, which can reduce image noise, as there are flocculent noises in polycrystalline solar cell images. Several experiments are conducted to observe the effect of different data augmentation methods on the ELPV dataset, especially the small-scale rotation and Gaussian blur. The setting of the baseline is the same as the above experiments, and different data augmentation methods are used on the images in the training set. No additional images are added to the training set. The results are shown in Table IV.

Not all image augmentation techniques can improve the performance of the model. A series of flipping and rotations has brought great improvement. Through the results of Gaussian blur, it can be seen that Gaussian blur with a blur radius of 1 can improve the performance. When the blur degree increases, which is a Gaussian blur with a blur radius of 2, the effect is not as good as the baseline. The reason is that the large degree of image blur can not only eliminate the noise interference but also severely blur the small defects. The combination augmentation of flipping, rotation, and Gaussian blur (radius = 1) operations is better than that of any single image augmentation operation, as shown in the bottom of Table IV.

## IV. CONCLUSION

Based on the observation of the EL dataset, a defective image generation approach based on the extraction of defective regions is proposed. To the best of the authors' knowledge, this article is the first work to provide deep research on the data imbalance problem in defect inspection for EL images of solar cells. There have been some research works working only on the defect inspection research of solar cells or only on the problem of data imbalance in the general domain, but the research that comprehensively considers the data imbalance problem in the solar cell defect inspection domain is still in the blank state.

Experiments demonstrate that the proposed method can provide more information for the model than commonly used oversampling and data augmentation, thus alleviating the imbalance of the EL dataset and improving the learning model's ability to inspect defects. Our method enables the rapid and flexible generation of a substantial quantity of defective images. Experiments verify that expanding the dataset by generating higher

quality defective samples to balance the distribution of samples is helpful. Future work can be conducted from this perspective to further improve the solar cell defect inspection performance under data imbalance.

## REFERENCES

[1] International Energy Agency, "Snapshot of global PV markets 2024," *Int. Energy Agency*, 2024. [Online]. Available: https://iea-pvps.org/snapshot-reports/snapshot-2024/

[2] C. Bhore et al., "Experimental investigation on minimizing degradation of solar energy generation for photovoltaic module by modified damping systems," *Sol. Energy*, vol. 250, pp. 194–208, Jan. 2023, doi: 10.1016/j.solener.2022.12.015.

[3] G. Badran and M. Dhimish, "Comprehensive study on the efficiency of vertical bifacial photovoltaic systems: A U.K. case study," *Sci. Rep.*, vol. 14, no. 1, Aug. 2024, Art. no. 18380, doi: 10.1038/s41598-024-68018-1.

[4] K. Bedrich et al.,, "Electroluminescence imaging of PV devices: Advanced vignetting calibration," *IEEE J. Photovolt.*, vol. 8, no. 5, pp. 1297–1304, Sep. 2018, doi: 10.1109/JPHOTOV.2018.2848722.

[5] D. Tsai, S. Wu, and W. Li, "Defect detection of solar cells in electroluminescence images using Fourier image reconstruction," *Sol. Energy Mater. Sol. Cells*, vol. 99, pp. 250–262, Apr. 2012, doi: 10.1016/j.solmat.2011.12.007.

[6] S. A. Anwar and M. Z. Abdullah, "Micro-crack detection of multicrystalline solar cells featuring an improved anisotropic diffusion filter and image segmentation technique," *EURASIP J. Image Video Process.*, vol. 2024, Mar. 2014, Art. no. 15, doi: 10.1186/1687-5281-2014-15.

[7] S. Deitsch et al., "Automatic classification of defective photovoltaic module cells in electroluminescence images," *Sol. Energy*, vol. 185, pp. 455–468, Jun. 2019, doi: 10.1016/j.solener.2019.02.067.

[8] A. M. Karimi et al., "Automated pipeline for photovoltaic module electroluminescence image processing and degradation feature classification," *IEEE J. Photovolt.*, vol. 9, no. 5, pp. 1324–1335, Sep. 2019, doi: 10.1109/JPHOTOV.2019.2920732.

[9] B. Su, H. Chen, and Z. Zhou, "BAF-Detector: An efficient CNN-based detector for photovoltaic cell defect detection," *IEEE Trans. Ind. Electron.*, vol. 69, no. 3, pp. 3161–3171, Mar. 2022, doi: 10.1109/TIE.2021.3070507.

[10] M. W. Akram et al., "CNN based automatic detection of photovoltaic cell defects in electroluminescence images," *Energy*, vol. 189, Dec. 2019, Art. no. 116319, doi: 10.1016/j.energy.2019.116319.

[11] S. Hassan and M. Dhimish, "Enhancing solar photovoltaic modules quality assurance through convolutional neural network-aided automated defect detection," *Renewable Energy*, vol. 219, no. 1, Dec. 2023, Art. no. 119389, doi: 10.1016/j.renene.2023.119389.

[12] S. Hassan and M. Dhimish, "Dual spin max pooling convolutional neural network for solar cell crack detection," *Sci. Rep.*, vol. 13, no. 1, Jul. 2023, Art. no. 11099, doi: 10.1038/s41598-023-38177-8.

[13] J. Fioresi et al., "Automated defect detection and localization in photovoltaic cells using semantic segmentation of electroluminescence images," *IEEE J. Photovolt.*, vol. 12, no. 1, pp. 53–61, Jan. 2022, doi: 10.1109/JPHOTOV.2021.3131059.

[14] M. Galar, A. Fernandez, E. Barrenechea, H. Bustince, and F. Herrera, "A review on ensembles for the class imbalance problem: Bagging-, boosting-, and hybrid-based approaches," *IEEE Trans. Syst. Man Cybern. Part C-Appl. Rev.*, vol. 42, no. 4, pp. 463–484, Jul. 2012, doi: 10.1109/TSMCC.2011.2161285.

[15] M. W. Akram et al.,, "Automatic detection of photovoltaic module defects in infrared images with isolated and develop-model transfer deep learning," *Sol. Energy*, vol. 198, pp. 175–186, Mar. 2020, doi: 10.1016/j.solener.2020.01.055.

[16] N. Zhang, S. Shan, H. Wei, and K. Zhang, "Micro-cracks detection of polycrystalline solar cells with transfer learning," *J. Phys. Conf. Ser.*, vol. 1651, Nov. 2020, Art. no. 012118, doi: 10.1088/1742-6596/1651/1/012118.

[17] X. Chen, T. Karin, and A. Jain, "Automated defect identification in electroluminescence images of solar modules*," *Sol. Energy*, vol. 242, pp. 20–29, Aug. 2022, doi: 10.1016/j.solener.2022.06.031.

[18] M. Y. Demirci, N. Besli, and A. Gumuscu, "Efficient deep feature extraction and classification for identifying defective photovoltaic module cells in electroluminescence images," *Expert Syst. Appl.*, vol. 175, Aug. 2021, Art. no. 114810, doi: 10.1016/j.eswa.2021.114810.

[19] B. Su, Z. Zhou, and H. Chen, "PVEL-AD: A large-scale open-world dataset for photovoltaic cell anomaly detection," *IEEE Trans. Ind. Informat.*, vol. 19, no. 1, pp. 404–413, Jan. 2023, doi: 10.1109/TII.2022.3162846.

[20] S. Ioffe and C. Szegedy, "Batch normalization: Accelerating deep network training by reducing internal covariate shift," in *Proc. 32nd Int. Conf. Mach. Learn.*, 2015, pp. 448–456.

[21] N. Srivastava, G. Hinton, A. Krizhevsky, I. Sutskever, and R. Salakhutdinov, "Dropout: A simple way to prevent neural networks from overfitting," *J. Mach. Learn. Res.*, vol. 15, pp. 1929–1958, Jun. 2014.

[22] M. Köntges et al., "Review of failures of photovoltaic modules final," Int. Energy Agency, 2014. [Online]. Available: https://iea-pvps.org/key-topics/review-of-failures-of-photovoltaic-modules-final/

[23] K. He, X. Zhang, S. Ren, and J. Sun, "Deep residual learning for image recognition," in *Proc. IEEE/CVF Conf. Comput. Vis. Pattern Recognit.*, 2016, pp. 770–778, doi: 10.1109/CVPR.2016.90.

[24] L. A. Jeni, J. F. Cohn, and F. De L. Torre, "Facing imbalanced data recommendations for the use of performance metrics," in *Proc. Humaine Assoc. Conf. Affect. Comput. Intell. Interact.*, 2013, pp. 245–251, doi: 10.1109/ACII.2013.47.

[25] V. Garcia, R. A. Mollineda, and J. S. Sanchez, "Index of balanced accuracy: A performance measure for skewed class distributions," in *Proc. Conf. Pattern Recognit. Image Anal.*, 2009, pp. 441–448.

[26] D. Chicco and G. Jurman, "The advantages of the Matthews correlation coefficient (MCC) over F1 score and accuracy in binary classification evaluation," *BMC Genomic.*, vol. 21, no. 1, Jan. 2020, Art. no. 6, doi: 10.1186/s12864-019-6413-7.

[27] H. Guo et al.,, "Logistic discrimination based on G-mean and F-measure for imbalanced problem," *J. Intell. Fuzzy Syst.*, vol. 31, no. 3, pp. 1155–1166, Jan. 2016, doi: 10.3233/IFS-162150.

[28] J. Zhang et al., "Automatic detection of defective solar cells in electroluminescence images via global similarity and concatenated saliency guided network," *IEEE Trans. Ind. Informat.*, vol. 19, no. 6, pp. 7335–7345, Jun. 2023, doi: 10.1109/TII.2022.3211088.

[29] C. Li, Y. Yang, S. Spataru, K. Zhang, and H. Wei, "A robust parametrization method of photovoltaic modules for enhancing one-diode model accuracy under varying operating conditions," *Renewable Energy*, vol. 168, pp. 764–778, May 2021, doi: 10.1016/j.renene.2020.12.097.

[30] Y. Shen et al., "Temperature estimation of partially shaded photovoltaic modules using a multiphysics model," *IEEE J. Photovolt.*, vol. 12, no. 5, pp. 1243–1251, Sep. 2022, doi: 10.1109/JPHOTOV.2022.3176440.

[31] A. M. Karimi et al., "Generalized and mechanistic PV module performance prediction from computer vision and machine learning on electroluminescence images," *IEEE J. Photovolt.*, vol. 10, no. 3, pp. 878–887, May 2020, doi: 10.1109/JPHOTOV.2020.2973448.

[32] J. Zhang, X. Chen, H. Wei, and K. Zhang, "A lightweight network for photovoltaic cell defect detection in electroluminescence images based on neural architecture search and knowledge distillation," *Appl. Energy*, vol. 355, Feb. 2024, Art. no. 122184, doi: 10.1016/j.apenergy.2023.122184.